

# Insertion of microneedles into skin: measurement and prediction of insertion force and needle fracture force

Shawn P. Davis<sup>a</sup>, Benjamin J. Landis<sup>a</sup>, Zachary H. Adams<sup>a</sup>,  
Mark G. Allen<sup>b</sup>, Mark R. Prausnitz<sup>a,\*</sup>

<sup>a</sup>*School of Chemical & Biomolecular Engineering, 311 Ferst Drive, Georgia Institute of Technology, Atlanta, GA 30332-0100, USA*

<sup>b</sup>*School of Electrical and Computer Engineering, Georgia Institute of Technology, Atlanta, GA 30332-0269, USA*

Accepted 10 December 2003

## Abstract

As a hybrid between a hypodermic needle and transdermal patch, we have used microfabrication technology to make arrays of micron-scale needles that transport drugs and other compounds across the skin without causing pain. However, not all microneedle geometries are able to insert into skin at reasonable forces and without breaking. In this study, we experimentally measured and theoretically modeled two critical mechanical events associated with microneedles: the force required to insert microneedles into living skin and the force needles can withstand before fracturing. Over the range of microneedle geometries investigated, insertion force was found to vary linearly with the interfacial area of the needle tip. Measured insertion forces ranged from approximately 0.1–3 N, which is sufficiently low to permit insertion by hand. The force required to fracture microneedles was found to increase with increasing wall thickness, wall angle, and possibly tip radius, in agreement with finite element simulations and a thin shell analytical model. For almost all geometries considered, the margin of safety, or the ratio of fracture force to insertion force, was much greater than one and was found to increase with increasing wall thickness and decreasing tip radius. Together, these results provide the ability to predict insertion and fracture forces, which facilitates rational design of microneedles with robust mechanical properties. © 2004 Elsevier Ltd. All rights reserved.

*Keywords:* Transdermal drug delivery; MEMS; Microfabrication; Penetration force; Skin mechanical properties

## 1. Introduction

Effectively transporting drugs into the body is a significant challenge (Park, 1997; Langer, 1998). Oral delivery of pills is the most common and convenient method, but is not always appropriate because drugs must survive the harsh environment of the gastrointestinal tract and first pass metabolism of the liver. More sensitive drugs, including proteins, are usually administered by hypodermic injection, which avoids the gastrointestinal tract but also causes pain and requires medical expertise. In addition, bolus delivery from conventional injections reduces the effectiveness of drugs that would benefit from controlled release over time.

As an alternative, transdermal patches provide convenient, time-release delivery that avoids the gastro-

intestinal tract (Bronaugh et al., 1999; Prausnitz, 2001). However, rates of delivery are often slow, because the skin's outer layer of stratum corneum severely limits diffusion of most compounds. For this reason, there are just a dozen drugs approved for transdermal delivery in the United States (Sifton, 2003).

As a hybrid of hypodermic needles and transdermal patches, arrays of micron-scale “microneedles” have been created to painlessly pierce the skin's stratum corneum and thereby transport drugs into the body (Henry et al., 1998). Over the past few years, a variety of different microneedle designs have been fabricated by employing the tools of the microelectronics industry using materials such as silicon, metals and polymers, with feature sizes ranging from sub-micron to millimeters (Chen and Wise, 1997; Brazzle et al., 1999; Lin and Pisano, 1999; McAllister et al., 2000; Stoeber and Liepmann, 2000; Griss et al., 2001). Solid microneedles have increased skin permeability in vitro by up to four orders of magnitude for compounds ranging from small

\*Corresponding author. Tel.: +1-404-894-5135; fax: +1-404-894-2866.

E-mail address: mark.prausnitz@che.gatech.edu (M.R. Prausnitz).

molecules to proteins to polystyrene nanospheres (McAllister et al., 2003). In vivo animal studies have further shown delivery of oligonucleotides (Lin et al., 2001) and vaccines (Matriano et al., 2002). Microinjection with hollow microneedles has demonstrated fluid transport in vitro (Stoeber and Liepmann, 2000) and insulin delivery in diabetic animals (McAllister et al., 2003). Microneedles have also been used to extract interstitial fluid from skin for glucose measurement (Mukerjee et al., 2003). Human studies demonstrated that microneedles can be inserted into skin without pain (Kaushik et al., 2001).

Although many microneedle designs have been proposed, not all are capable of inserting into the skin. To provide quantitative predictions of microneedle insertion, in this study we have experimentally measured and theoretically modeled the effect of microneedle geometry on the force required to insert microneedles into the skin of human subjects and the force needles can withstand before fracturing. Understanding these relationships will allow intelligent design of needles that penetrate with small applied force and are strong enough to withstand this force.

To our knowledge, the mechanics of microneedle insertion into the skin of human subjects has not been studied before. Studies using cadavers measured the force to insert conventional hypodermic needles in the context of physician training (Brett et al., 1997; Frick et al., 2001). Other studies measured microneedle insertion force into synthetic polymer sheets (Chandrasekaran and Frazier, 2002; Stupar and Pisano, 2001). To our knowledge, no previous studies quantitatively determined the effect of needle geometry on insertion force.

Similarly, measuring the mechanical strength of microneedles has received limited attention. The few quantitative measurements available are for “large” microneedles measuring millimeters in length, where buckling is the primary mode of failure (Oka et al., 2001; Chandrasekaran and Frazier, 2002; Stupar and Pisano, 2001). For the sub-millimeter needles examined in this study, fracture was caused by exceeding the ultimate stress of the needle material (see below). To our knowledge, no previous studies have quantitatively determined the effect of needle geometry on fracture force.

## 2. Materials and methods

### 2.1. Fabrication of microneedles

Microneedles were created with the tools of the microelectronics industry using a modified LIGA process (Davis et al., 2003). Briefly, an excimer laser (Micromaster, Resonetics, Nashua, NH) drilled the

desired microneedle geometry through a polyethylene terephthalate sheet (Mylar, Dupont, Wilmington, DE) measuring 500 or 720  $\mu\text{m}$  thick, which determined the microneedle height.

This mold was then made electrically active using a seed layer of Ti (350 nm)/Cu (6500 nm)/Ti (350 nm) deposited using direct current sputtering (Model 601, CVC, Rochester, NY). The upper layer of titanium was removed using 2% hydrofluoric acid just prior to electroplating to expose the copper layer, which was then electroplated in a Watts nickel bath (Technic, Cranston, RI) to create the microneedle array. The current density (10 mA/cm<sup>2</sup>) and plating duration (30–120 min) determined the thickness of the metal walls and base.

Finally, the polymer mold was dissolved in a 1 N solution of boiling NaOH and the copper seed layer was removed using a saturated solution of cupric sulfate in ammonia. The completed microneedles were cleaned using the organic step of the RCA cleaning procedure (1:1:5 H<sub>2</sub>SO<sub>4</sub>:H<sub>2</sub>O<sub>2</sub>:H<sub>2</sub>O at 80°C) for 15 min. A representative microneedle is shown in Fig. 1.

### 2.2. Characterization of microneedle geometry

Prior to testing, all microneedles were imaged by scanning electron microscopy (Hitachi 3500, Pleasanton, CA) to determine their base radius, tip radius, and wall thickness. Interfacial area (i.e. the effective area of contact between the needle and the skin) was then calculated in two ways: (i) the annular surface area,  $A_a$ , at the needle tip

$$A_a = \pi \left( r_t t - \frac{t^2}{4} \right) \quad (1)$$

and (ii) the full cross-sectional area,  $A_f$ , at the needle tip

$$A_f = \pi r_t^2. \quad (2)$$

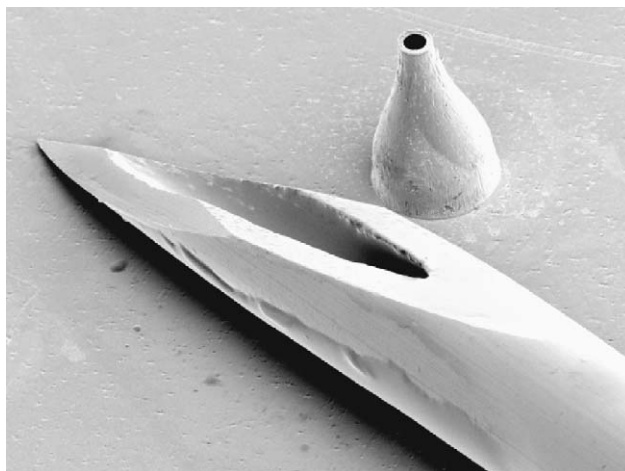


Fig. 1. Scanning electron micrograph of a 500- $\mu\text{m}$  tall microneedle next to the tip of a 27 gauge hypodermic needle.

Needle wall angle,  $\alpha$ , was calculated as

$$\alpha = \tan^{-1} \left( \frac{r_b - r_t}{h} \right), \quad (3)$$

where  $r_t$  is the outer radius of the microneedle tip,  $r_b$  is the outer radius at the needle base,  $t$  is the wall thickness, and  $h$  is the height.

### 2.3. Measurement of insertion force into human skin

A displacement–force test station (Model 921A, Tricor Systems, Elgin, IL) was used to measure the force applied to a needle, needle position, and skin resistance during the sequence of the needle's translation to the skin, deflection of tissue around the needle, and insertion into the skin of human subjects. Because visual observation of needle insertion was extremely difficult, a drop in electrical resistance of the skin was used to identify needle penetration. The electrical resistance of skin's outermost layer, stratum corneum, is much greater than deeper tissues (Yamamoto and Yamamoto, 1976), so that skin resistance drops dramatically as soon as a needle penetrates. A similar technique was used by Young et al. (1987) to monitor needle insertion into deeper tissues during epidural block procedures.

Prior to testing, microneedles were first cleaned by immersion in 70% ethanol for 15 min. To electrically and mechanically connect a microneedle to the displacement–force test station, a 30-gauge copper wire was first soldered to the base of the microneedle. The base was then mechanically reinforced with adhesive tape (Blenderm, 3M, Saint Paul, MN) and fixed to a 3-mm diameter brass post (McMaster-Carr, Atlanta, GA) using cyanoacrylate adhesive (Loctite, Rocky Hill, CT). The post/microneedle assembly was inserted into the test station probe and the electrical connection between the test station and microneedle was made to the soldered wire.

Microneedle insertion tests were performed on three Caucasian male subjects who ranged in age from 20 to 26 years old and gave informed consent. The protocol was approved by the Georgia Institute of Technology Institutional Review Board.

Each subject was seated at the test station and his hand was fully hydrated by immersion in warm water for 5 min. After drying the hand, a counter electrode made of Ag–AgCl (In Vivo Metric, Healdsburg, CA) was affixed to the back of the hand with adhesive tape (Shamrock, Bellwood, IL) on a section of skin that was either mechanically stripped of stratum corneum using a scalpel blade or treated with electrode gel (Spectra 360, Parker, Fairfield, NJ) to ensure low-resistance electrical contact. To improve electrical contact between the skin and the microneedle, a single drop of physiological saline was placed at the insertion point, which was

always located within a 1 cm<sup>2</sup> site at the proximal base of the knuckle.

To measure needle force, needle displacement, and skin resistance associated with needle insertion, the test station pressed the microneedle against the subject's hand at a rate of 1.1 mm/s until a preset maximum load of 500 g was reached. All microneedles used for insertion testing were 720  $\mu\text{m}$  tall. Tip radius and wall thickness were varied over 30–80  $\mu\text{m}$  and 5–58  $\mu\text{m}$ , respectively.

### 2.4. Measurement of fracture force

The force required for mechanical fracture of a microneedle was tested under an axial compression load using an axial load test station (ScopeTest1, EnduraTEC, Minnetonka, MN) that drove the microneedle against a flat block of aluminum at a rate of 0.01 mm/s until a preset displacement of 500  $\mu\text{m}$  was reached. Microneedles were attached to the testing surface using adhesive tape (Shercon, Santa Fe Springs, CA) around the base of the needle. Microneedle fracture was observed through an attached microscope to evaluate the mode of failure. The force and displacement data were used to quantitatively determine the fracture force.

All microneedles used for mechanical fracture testing were 500  $\mu\text{m}$  tall. Studies varying tip radius had constant wall thickness of 12  $\mu\text{m}$  and wall angle of 78.5°. Studies varying wall thickness had constant tip radius of 43  $\mu\text{m}$  and wall angle of 78.5°. Studies varying wall angle had constant tip radius of 30  $\mu\text{m}$  and wall thickness of 10  $\mu\text{m}$ . Base radius was not independently varied because stress is expected to maximize at the needle tip (Roark and Young, 1975), as confirmed by our visual observation of needle fracture at the tip (data not shown).

As a companion to fracture measurements, the intrinsic mechanical properties of electroplated nickel were determined with the same axial load test station using “dog bone” shaped structures (Sharpe et al., 1997) electroplated into polymer molds with the same plating conditions and nickel bath as used for microneedle fabrication. The cross-section of the central test region of the dog bone measured 200  $\mu\text{m} \times 35 \mu\text{m}$ . These structures were tested under the same conditions as the microneedles, except that tensile loads were applied rather than compressive loads, and cyanoacrylate adhesive was used to fix the samples rather than tape. To eliminate the possibility of buckling failure, ultimate stress is commonly determined using tensile testing and is expected to yield values applicable to compressive stresses (Beer and Johnston, 1992).

Using this approach, the ultimate stress of our electroplated nickel was found to be 1.2 GPa. As expected, this value exceeds bulk nickel's ultimate stress of 0.32 GPa (Davis, 1998) and is closer to literature values for electroplated nickel from sulfamate baths of 0.5–0.8 GPa (Mazza et al., 1996; Sharpe et al., 1997).

### 3. Theory

#### 3.1. Force of insertion

To predict the force required for insertion into skin based on microneedle geometry, we postulated that when the energy delivered to the skin by the needle exceeds the energy necessary to create a tear in the skin, the needle will insert into the skin. Pereira et al. (1997) used a similar approach to model tears in the skin initiated and propagated with scissors in vitro. In this case the stored potential energy released during cracking was set equal to the surface energy of new surfaces created. Eq. (4) relates the work necessary to initiate a crack per unit area, referred to as crack fracture toughness,  $G_c$ , to the total work input to propagate the crack,  $\delta W$ , and the surface area of the new fracture,  $\delta A$

$$G_c = \left( \frac{\delta W}{\delta A} \right)_U. \quad (4)$$

For microneedles, we were interested in the energy to puncture the skin rather than the energy to propagate a fracture. Therefore, the work input, which was related to the change in potential energy between unaltered skin and the skin just prior to needle penetration, was calculated as the area under the load versus displacement curve before fracture as opposed to the area after fracture in the case of crack propagation (Gurney and Hunt, 1967).

In this case,  $\delta W = \int F dx$ , where  $F$  is the force applied by the needle,  $x$  is the axial position of the needle, and the boundaries of integration are from the point of needle contact with the skin to the point of needle insertion. Correspondingly, the change in fracture area is the difference between the puncture area prior to insertion (i.e., zero) and the area after puncture (i.e., the area of contact between the needle and the skin, which we have called the interfacial area of the needle,  $A$ ). Eq. (4) can therefore be rewritten as

$$\int_{x=0}^{x=x_i} F dx = G_p A, \quad (5)$$

where  $G_p$  is the puncture fracture toughness and  $x_i$  is the displacement where insertion occurs. The left-hand side of Eq. (5) is the summation of work applied to the skin during its deflection. The right side of the equation is the work required to initiate a tear in the skin.

To calculate the summation of work applied to skin during its deflection, the relationship between force and displacement of skin was fitted empirically using an exponential equation

$$F = \theta e^{\tau x}, \quad (6)$$

where  $\theta$  is the pre-exponential constant and  $\tau$  is the exponential constant. Our data were fitted very well

using this approach ( $r^2 = 0.99$ ) and produced a value of  $\tau = 6.25 \pm 0.6 \text{ mm}^{-1}$  (data not shown).

Inserting Eq. (6) into Eq. (5) yields

$$\int_{x=0}^{x=x_i} \theta e^{\tau x} dx = G_p A, \quad (7)$$

$$\frac{\theta e^{\tau x_i}}{\tau} - \frac{\theta}{\tau} = G_p A, \quad (8)$$

$$F_i = \tau G_p A + \theta, \quad (9)$$

where  $F_i$  is force upon penetration into skin (i.e., insertion force). Eq. (9) predicts that insertion force should depend linearly on needle tip area. Moreover, having already determined the value for  $\tau$ , the slope of a graph of insertion force versus needle tip area can be used to determine  $G_p$ .

#### 3.2. Force of fracture

To predict the force required to fracture a micro-needle based on needle geometry, we developed both analytical and finite element modeling approaches. We first developed analytical predictions of fracture due to stresses in the structure exceeding the ultimate stress of the constituent material and due to buckling caused by elastic instability of the structure.

To predict the force required for fracture due to failure of the constituent material, we modeled micro-needles as thin shells (Roark and Young, 1975)

$$F_f = 2\pi r_t t \sigma_u \sin \alpha, \quad (10)$$

where  $F_f$  is the axial force required for needle fracture,  $r_t$  is the radius at the needle tip,  $t$  is the wall thickness,  $\sigma_u$  is the ultimate stress of the needle material (1.2 GPa, see above), and  $\alpha$  is the needle wall angle. This approach assumes needles fail when the membrane stress generated in the plane of the needle walls exceeds the ultimate stress of the needle material. Failure due to shear forces were neglected in this analysis because their contribution should be negligible for the relatively weakly tapered geometries used (i.e.,  $\alpha = 60\text{--}80^\circ$ ).

The thin-shell assumption used in Eq. (10) requires the ratio of tip radius to wall thickness to be greater than ten, which assures a uniform stress distribution across the wall thickness (Roark and Young, 1975). Because the microneedle geometries used in this study had radius-to-thickness ratios of 2.5–10.5, the thin-shell assumption is generally invalid. This means that predictions generated by this model overestimate fracture forces because they do not account for heterogeneous peak stresses and stresses normal to the plane of the needle walls. As discussed below, computational methods were used to account more fully for complex stress distributions.

To predict the force required for needle failure due to buckling, Hausrath and Dittoe (1962) have developed a

widely used empirical modification to an analytical solution

$$F_b = 0.277(2\pi Et^2 \sin^2 \alpha), \quad (11)$$

where  $F_b$  is the axial load to cause buckling and  $E$  is the Young's modulus of the structure's material (200 GPa, Sharpe et al., 1997).

Comparison of fracture force predictions by constituent material failure (Eq. (10)) and buckling modes (Eq. (11)) indicated that buckling should only occur when wall thickness is less than 1–2  $\mu\text{m}$  (data not shown). Because microneedle wall thickness in this study was at least 5  $\mu\text{m}$ , the buckling mode of failure was excluded from our analysis. This conclusion is consistent with visual observations during experimental studies of needle fracture, where the observed failure consistently involved collapse at the tip (i.e., material failure) and not bending at some location on the needle shaft (i.e., buckling) (data not shown).

As a companion to analytical solutions, we also predicted the force of microneedle failure using finite element simulations. These simulations accounted for all stresses within the needle wall regardless of their orientation or distribution, but required longer computation times and therefore additional effort to generate continuum predictions.

Simulations using ANSYS (Canonsburg, PA) were employed to solve for the von Mises stress (sum of stress in all directions) in cones with geometries matching the tested microneedles using three-dimensional models composed of tetrahedral elements. Simulations were solved for cones as an approximation of the fabricated needles which deviate slightly from this ideal geometry (Fig. 1). The force applied to a microneedle was varied iteratively until the simulation predicted a stress equal to the microneedle ultimate stress of the microneedle constituent material (i.e., 1.2 GPa) in a single element. Because a region of the needle larger than a single point exceeding the ultimate stress might be required for needle failure, simulation predictions may underestimate fracture force.

## 4. Results and discussion

### 4.1. Force of insertion

To determine the effect of microneedle geometry on the force required to insert microneedles into skin, single microneedles were pressed into the skin of human subjects while continuously measuring needle force and displacement, as well as skin resistance, which served to identify the point of needle penetration.

Fig. 2 shows representative data collected during the insertion of a microneedle into skin on the hand of a human subject. The force required to press the needle

against the skin increased with needle displacement, then showed a discontinuity upon insertion into the skin, and finally increased further when pressed deeper into the skin. The steep slope observed after insertion was probably caused by deflection limited by supporting bone structure beneath the test site and contact of the microneedle base and mounting post with the skin surface.

Fig. 2 also shows that as the needle was pressed against the skin, resistance of the needle-skin circuit decreased and then leveled off as the needle came into close contact with the skin. Upon insertion, skin resistance rapidly dropped and then slowly decreased further when pressed deeper. Because the discontinuity in the force curve was not always as dramatic as shown in Fig. 2, we used the more reliable drop in resistance to identify when needle insertion occurred.

Using this approach, insertion force was measured for microneedles with tip radius of 30 to 80  $\mu\text{m}$  and wall thickness of 5  $\mu\text{m}$  to solid tips (equivalent to 58  $\mu\text{m}$  wall thickness). As shown in Fig. 3, forces of insertion ranged from 0.08 to 3.04 N (i.e., 8–304 g). When plotted versus microneedle interfacial area, insertion force increased linearly, albeit with considerable scatter. A linear fit of the data ( $r^2 = 0.81$ ) yields

$$F_i = 0.00019A_f - 0.66, \quad (12)$$

where  $F_i$  has units of N and  $A_f$  is the full cross-sectional area of the needle (Eq. (2)) and has units of  $\mu\text{m}^2$ .

Theoretical considerations suggested that insertion force should depend linearly on interfacial area (see Section 3.1). However, it was not clear whether the area should be calculated as the annular ring of metal at the needle tip (Eq. (1)) or the full cross-sectional area at the tip, independent of lumen size (Eq. (2)). If the skin deformed conformally around the inner and outer walls

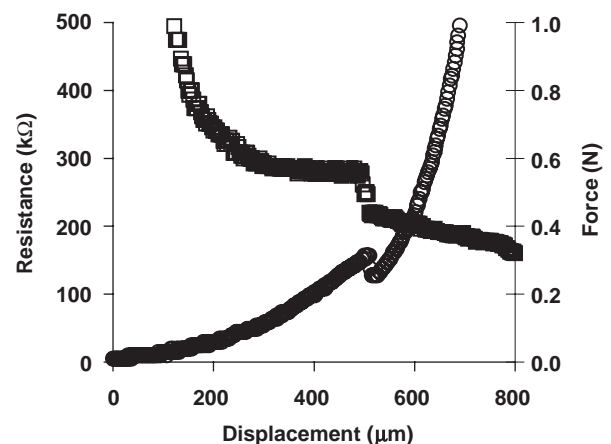


Fig. 2. Representative measurement of needle force (circle) and skin resistance (square) during microneedle displacement and insertion into the skin of a human subject. The point of insertion is identified by the sudden decrease in skin electrical resistance and the discontinuity in applied force.

of the microneedle, the area of contact would be annular in shape. If the skin was insufficiently flexible to dimple into the needle lumen and deformed only around the outer walls, the area of contact would be better described by the full cross-sectional area.

Statistical analysis of our data set using a two-way ANOVA suggested that insertion force depended significantly on the outer radius of the needle tip ( $p < 0.05$ ), but did not depend on wall thickness ( $p = 0.45$ ). The non-significant role of wall thickness suggests that the skin did not conform closely to the needle wall and therefore full cross-sectional area is the appropriate interfacial area. To further elucidate the effect of wall thickness, insertion force for hollow microneedles with a tip radius of  $58 \mu\text{m}$  and wall thickness of  $14\text{--}17 \mu\text{m}$  (i.e., with a hollow lumen radius of  $41\text{--}44 \mu\text{m}$ ) was compared to solid microneedles with tip radius of  $58 \mu\text{m}$  (i.e., no lumen). The average insertion force for hollow microneedles ( $1.65 \pm 0.03 \text{ N}$ ) was indistinguishable from the insertion force for solid microneedles ( $1.29 \pm 0.04 \text{ N}$ ) (Student's  $t$ -test,  $p = 0.06$ ), which further suggests that the full cross-sectional area better represents the skin-microneedle interface. Note that although the statistical significance is not strong, the average insertion force for hollow needles was greater than for solid needles, which is opposite to the expected behavior if skin were to deform into the microneedle lumen.

Consistent with theoretical predictions, Fig. 3 suggests a linear dependence of insertion force on interfacial area. Eqs. (9) and (12) can therefore be used to estimate the puncture toughness of skin as  $G_p = 30.1 \pm 0.6 \text{ kJ/m}^2$ . This estimate of puncture toughness (i.e., to initiate a defect in skin structure) can be compared to a Purslow's

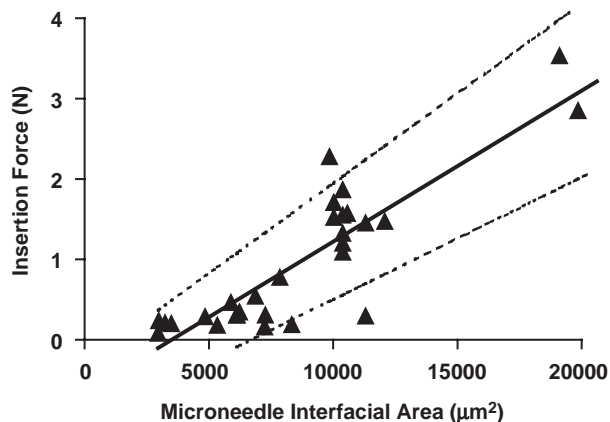


Fig. 3. Force of microneedle insertion into skin as a function of interfacial area. Insertion force increased with area of the microneedle–skin interface. The solid line shows a linear regression of the data (Eq. (12)). The upper and lower 95% confidence intervals are plotted as dashed lines. The interfacial area was calculated as the full cross-sectional area of the tip,  $A_f$  (see text). Data were collected from three human subjects as single data points ( $n = 1$ ).

(1983) measurement of rat skin fracture toughness made by tear testing (i.e., to expand an existing defect) of  $26.9 \pm 2.73 \text{ kJ/m}^2$ . Although rat skin differs from human skin (e.g., it is approximately one-third thinner), the mechanical properties of these two mammalian tissues are similar (Bronaugh et al., 1982). The agreement between these measurements of crack formation and crack propagation may be explained by the importance of the crack blunting effect of a viscoelastic material in both cases. In contrast, our measurements are an order of magnitude greater than those taken by Pereira (1997) from fracture toughness (i.e., crack propagation) during scissors cutting test,  $1.7 \pm 0.6 \text{ kJ/m}^2$ , in which the cutting edge of the blade reduces the effect of crack blunting due to the viscoelastic behavior.

#### 4.2. Force of fracture

The analysis presented until this point has considered the desirable outcome of needle insertion into skin. Fig. 4A shows an intact microneedle and Fig. 4B shows the cross-section of a microneedle inserted and embedded in a piece of cadaver skin. The skin surface has partially deformed around the needle, but a portion of

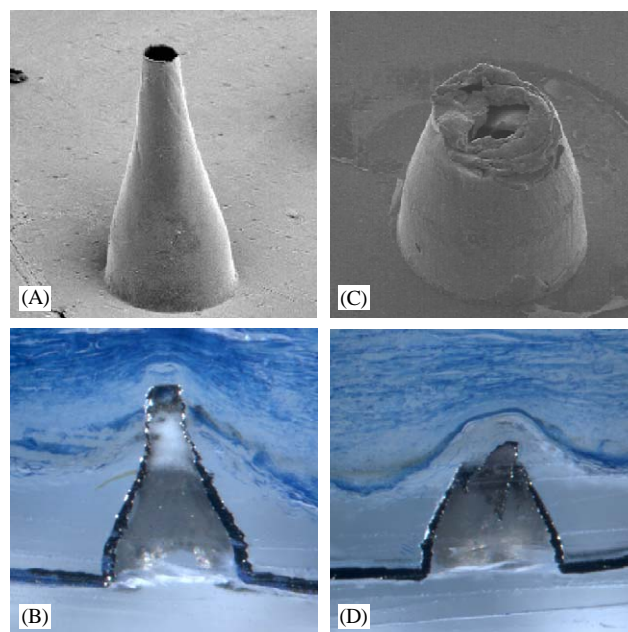


Fig. 4. Representative microscopic images of microneedles. (A) An intact microneedle. (B) A cross-sectional image of an intact microneedle inserted into cadaver skin. (C) A fractured microneedle after being pressed against a rigid surface. (D) A cross sectional image of a microneedle that deflected the skin, but fractured before inserting into an intact piece of cadaver skin. (A) and (C) are scanning electron micrographs. (B) and (D) are brightfield micrographs of microneedle–skin samples prepared by methyl methacrylate resin embedding of the tissue (Bancroft and Gamble, 2002). Cadaver tissue used in this study was frozen and subsequently thawed to room temperature before needle insertion; chemical preservatives were not used.

the needle has inserted into the skin. We expect that similar behavior occurred during insertion into living human subjects. Fig. 4C shows an undesirable outcome resulting from a mechanically weak microneedle. In this case, a microneedle was pressed against a rigid surface until it fractured. As a companion image, Fig. 4D shows a microneedle that was pressed against cadaver skin, but fractured before it could penetrate, leaving behind an intact piece of skin. Such needle failure did not occur in any of the human subject data presented in Fig. 3.

To determine the force of microneedle fracture as a function of needle geometry, we pressed a test block against the tips of microneedles until they fractured. Fig. 5 shows representative data in which the axial force applied to the needle increased with the block's displacement until the ultimate load of the microneedle was reached and it fractured, which was indicated by a discontinuity in the applied force and confirmed by visual observation during the test. After fracture, the block continued to press against the crushed microneedle with a load substantially lower than the ultimate load experimentally determined. Fig. 6 shows the dependence of microneedle fracture force on needle geometry. Over the range considered, fracture force did not depend tip radius (Fig. 6A,  $p = 0.93$ ), but increased with increasing wall thickness (Fig. 6B,  $p < 0.001$ ) and wall angle (Fig. 6C,  $p < 0.05$ ).

As a companion to experimental measurements, analytical and finite element models were developed to predict the fracture force. The analytical model was expected to overpredict fracture force because it did not account for peak stresses or stresses out of the plane. The finite element model took into account all stresses and stress non-uniformities, but was expected to underpredict due to the conservative failure criterion of exceeding the ultimate stress in just one grid element.

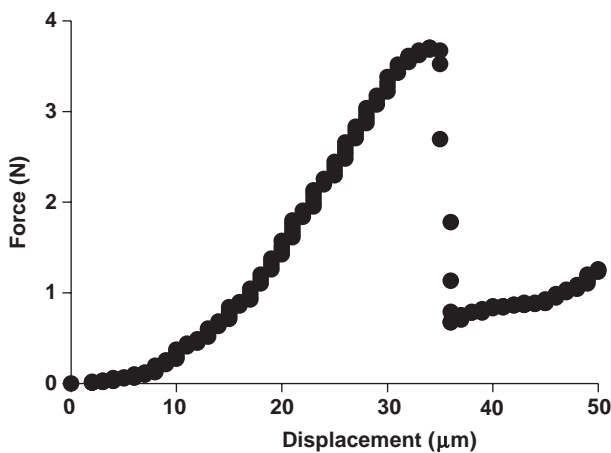


Fig. 5. Representative measurement of needle force during microneedle displacement and fracture under axial load. The discontinuity marks the fracture of the microneedle.

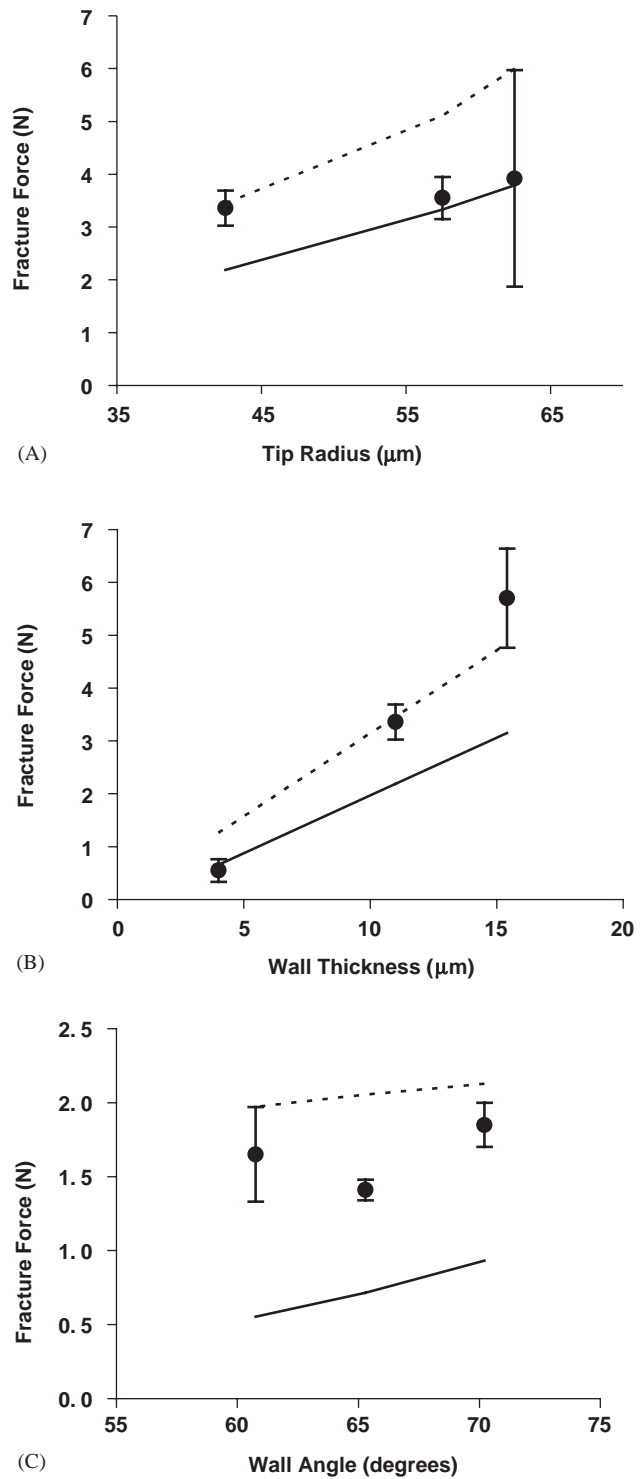


Fig. 6. Force of microneedle fracture as a function of needle geometry: (A) tip radius, (B) wall thickness, and (C) wall angle. Experimental data are shown as averages  $\pm$  standard deviation. Thin shell analytical solutions (Eq. (10)) are presented as dashed lines and ANSYS finite element simulation predictions are shown as solid lines.

Fig. 6 shows a comparison between analytical (dashed line) and finite element (solid line) predictions and experimental data. In the case of tip radius, both modeling approaches predict a moderate increase in

fracture force with increasing tip radius, although the data do not show this trend (Fig. 6A). Increasing tip radius is expected to increase the area over which the applied force is distributed resulting in lower stresses. The finite element model underpredicted the fracture force data by an average of 15% while the analytical solution overpredicted the fracture force by 33%.

In the case of wall thickness, both modeling approaches predict a sharp increase in fracture force with increasing wall thickness, in agreement with experimental data (Fig. 6B). Increasing wall thickness is expected to increase the area over which the applied force is distributed, resulting in lower stresses. As the wall thickness continued to increase, the measured fracture force increased more sharply than either model predicted. The average difference between the finite element simulation and fracture force was 33%, while the analytical solution differed by 49%.

Finally, in the case of wall angle, both the finite element and analytical models indicated that fracture force should modestly increase with increasing wall angle, in general agreement with experimental data (Fig. 6C). As the wall angle approaches vertical, and the shape of the needle approaches a cylinder, a larger portion of the total stress should become oriented along the plane of the microneedle wall, as opposed to normal to the wall, which results in an increased force of fracture. The finite element model underpredicted the fracture force by an average of 55% while the analytical solution differed by 27%.

#### 4.3. Margin of safety

Considered separately, the data and models of insertion force and fracture force have value, but combining these analyses permits identifying needle geometries with appropriate margins of safety between insertion force and fracture force (Fig. 7). The upper plane in Fig. 7A represents the force necessary to fracture a microneedle as predicted by the analytical solution (which provided more accurate estimates than finite element predictions). The lower plane represents the upper 95% interval of the insertion force as predicted by the fitted puncture resistance value (a conservative upper estimate).

Fig. 7B shows the margin of safety (i.e., ratio) between the fracture and insertion forces of microneedles. This analysis indicates that microneedles with small radius and large wall thickness offer the greatest margin of safety between insertion and fracture force, where insertion forces were many times smaller than fracture forces. Small tip radius significantly reduces insertion force and only modestly reduces fracture force, whereas large wall thickness dramatically increases fracture force and has no effect on insertion force over the range of geometries considered.

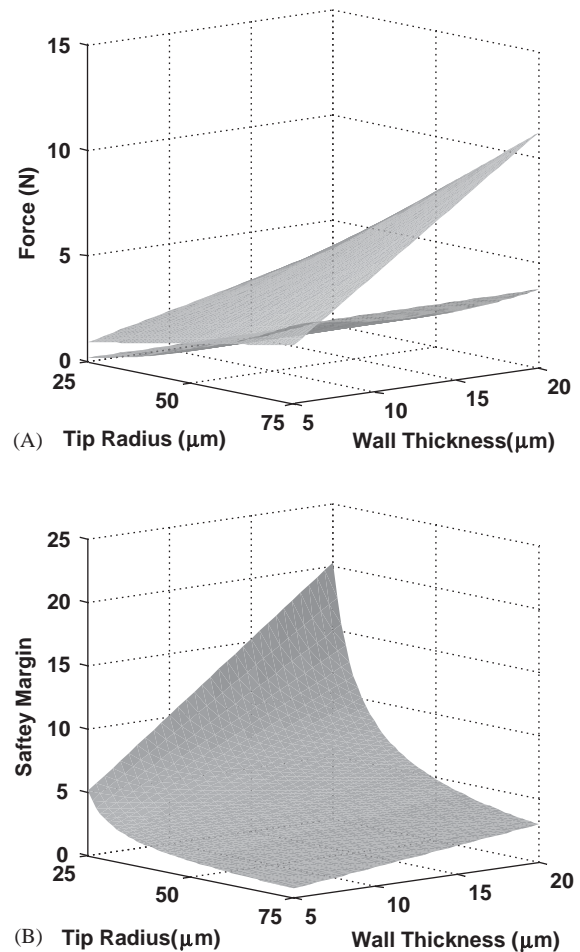


Fig. 7. (A) Comparison of insertion force to fracture force and (B) safety margin between insertion and fracture forces of the microneedles. In (A), the upper surface is the analytical solution for the microneedle fracture force (Eq. (10)), and the lower plane is the insertion force at the 95% confidence level. In (B), margins of safety were generally much greater than one, where larger tip radius and wall thickness increased safety margins.

## 5. Conclusions

In conclusion, experimental measurements and theoretical modeling have shown that microneedle insertion force increases as a linear function of needle tip cross-sectional area. Measured insertion forces of 0.1–3 N were sufficiently low to permit insertion by hand. Data analysis suggests that skin does not deform into the lumen of hollow needles during insertion. Theoretical and experimental analysis of needle fracture suggests that fracture forces increase strongly with increasing wall thickness and may increase modestly with increasing wall angle and tip radius. Comparison of insertion forces to fracture forces showed that fracture forces were almost always greater than insertion forces over the range of geometries considered and that margins of safety of at least five-fold could be achieved using needles of small tip radius and large wall thickness. The

results of this study can be used to rationally design microneedles that easily insert into skin without breaking for novel uses in transdermal drug delivery and other applications.

## Acknowledgements

This work was funded in part by the National Institutes of Health. The authors would like to thank the staff of the Georgia Tech Microelectronics Research Center for assistance during fabrication of microneedles and Jianmin Qu for helpful discussions on skin and needle mechanics.

## References

- Bancroft, J.D., Gamble, M., 2002. *Theory and Practice of Histological Techniques* 5th ed.. Churchill Livingstone, London.
- Beer, F.P., Johnson, E.R., 1992. *Mechanics of Materials* 2nd Ed. McGraw-Hill, New York.
- Brazzle, J., Papautsky, I., Frazier, A.B., 1999. Micromachined needle arrays for drug delivery or fluid extraction. *IEEE Engineering in Medicine and Biological Magazine* 18, 53–58.
- Brett, P.N., Parker, T.J., Harrison, A.J., Thomas, T.A., Carr, A., 1997. Simulation of resistance forces acting on surgical needles. *Proceedings of the Institute of Mechanical Engineering Part H* 211, 335–347.
- Bronaugh, R.L., Maibach, H.I., (Eds.), 1999. *Percutaneous Absorption: Drugs–Cosmetics–Mechanisms–Methodology*. 3rd ed., Marcel Dekker, New York.
- Bronaugh, R.L., Stewart, R.F., Conodon, E.R., 1982. Methods for in vitro Percutaneous Absorption Studies II. *Animal Models for Human Skin. Toxicology and Applied Pharmacology* 62, 481–488.
- Chandrasekaran, S., Frazier, A.B., 2002. An autonomous, microneedle-based bio-analysis system. In: *Proceedings of the 2nd Joint EMBS-BMES Conference*. Houston, TX, pp. 1644–1645.
- Chen, J., Wise, K.D., 1997. A multichannel neural probe for selective chemical delivery at the cellular level. *IEEE Transactions on Biomedical Engineering* 44, 760–769.
- Davis, J.R. (Ed.), 1998. *Metals Handbook*. 2nd ed., ASM International, Materials Park, OH.
- Davis, S.P., Prausnitz, M.R., Allen, M.G., 2003. Fabrication and characterization of laser micromachined hollow microneedles. In: *Proceedings of the 12th International Conference on Solid-State Sensors and Actuators*, Boston, MA, pp. 1435–1438.
- Frick, T.B., Marucci, D.D., Cartmill, J.A., Martin, C.J., Walsh, W.R., 2001. Resistance forces acting on suture needles. *Journal of Biomechanics* 34, 1335–1340.
- Griss, P., Enoksson, P., Tolvanen-Laakso, H.K., Merilainen, P., Ollmar, S., Stemme, G., 2001. Micromachined electrodes for biopotential measurements. *Journal of Microelectromechanical Systems* 10, 10–16.
- Gurney, C., Hunt, J., 1967. Quasi-static crack propagation. *Proceedings of the Royal Society of London A* 299, 508–524.
- Hausrath, A.H., Dittoe, F.A., 1962. Development of design strength levels for the elastic stability of monocoque cones under axial compression. *Collected Papers on Instability for Shell Structures*, National Aeronautics and Space Administration, Technical Note, D-1510, pp. 45–56.
- Henry, S., McAllister, D.V., Allen, M.G., Prausnitz, M.R., 1998. Microfabricated microneedles: a novel approach to transdermal drug delivery. *Journal of Pharmaceutical Science* 87, 922–925.
- Kaushik, S., Hord, A.H., Denson, D.D., McAllister, D.V., Smitra, S., Allen, M.G., Prausnitz, M.R., 2001. Lack of pain associated with microfabricated microneedles. *Anesthesia and Analgesia* 92, 502–504.
- Langer, R., 1998. Drug delivery and targeting. *Nature* 392, 5–10.
- Lin, L., Pisano, A.P., 1999. Silicon-processed microneedles. *IEEE Journal of Micromechanical Systems* 8, 78–84.
- Lin, W., Cormier, M., Samiee, A., Griffin, A., Johnson, B., Teng, C.L., Hardee, G.E., Daddona, P.E., 2001. Transdermal delivery of antisense oligonucleotides with microprojection patch (Macroflux<sup>®</sup>) technology. *Pharmaceutical Research* 18, 1789–1793.
- Matriano, J.A., Cormier, M., Johnson, J., Young, W.A., Buttery, M., Nyam, K., Daddona, P.E., 2002. Macroflux<sup>®</sup> microprojection array patch technology: a new and efficient approach for intracutaneous immunization. *Pharmaceutical Research* 19, 63–70.
- McAllister, D.V., Allen, M.G., Prausnitz, M.R., 2000. Microfabricated microneedles for gene and drug delivery. *Annual Review on Biomedical Engineering* 2, 289–313.
- McAllister, D.V., Wang, P.M., Davis, S.P., Park, J.H., Allen, M.G., Prausnitz, M.R. Microfabricated needles for transdermal delivery of macromolecules and nanoparticles: fabrication methods and transport studies. *Proc. Nat. Acad. Sci. (USA)* 100, 13755–13760.
- Mazza, E., Abel, S., Dual, J., 1996. Experimental determination of mechanical properties of Ni and Ni–Fe microbars. *Microsystem Technologies* 2, 197–202.
- Mukerjee, E.V., Issseroff, R.R., Collins, S.D., Smith, R.L., 2003. Microneedle array with integrated microchannels for transdermal sample extraction and in situ analysis. In: *Proceedings of the 12th International Conference on Solid-State Sensors and Actuators*, Boston, MA, pp. 1439–1441.
- Oka, K., Aoyagi, S., Isono, Y., Hashiguchi, G., Fujita, H., 2001. Fabrication of a micro needle for a trace blood test. In: *Proceedings of the 11th International Conference on Solid-State Sensors and Actuators*, Munich, Germany, pp. 412–415.
- Park, K. (Ed.), 1997. *Controlled Drug Delivery: Challenges and Strategies*. American Chemical Society: Washington, DC.
- Pereira, B.P., Lucas, P.W., Swee-Hin, T., 1997. Ranking the fracture toughness of thin mammalian soft tissues using the scissors cutting test. *Journal of Biomechanics* 30, 91–94.
- Prausnitz, M.R., 2001. Overcoming skin's barrier: the search for effective and user-friendly drug delivery. *Diabetes Technology Therapy* 3, 233–236.
- Purslow, P.P., 1983. Measurement of the fracture toughness of extensible connective tissues. *Journal of Material Science* 18, 3591–3598.
- Roark, R.J., Young, W.C., 1975. *Formulas for Stress and Strain*. 5th Ed., McGraw-Hill, New York, pp. 446–456, 548–563.
- Sharpe, W.N., LaVan, D.A., McAleavey, A., 1997. Mechanical properties of LIGA deposited nickel for MEMS transducers. In: *Proceedings of the 8th International Conference on Solid-State Sensors and Actuators*, Chicago, IL, pp. 607–610.
- Sifton, D.W. (Ed.), 2003. *Physicians' Desk Reference*, 52nd ed., Thomson PDR, Montvale, NJ.
- Stoeber, B., Liepmann, D., 2000. Fluid injection through out-of-plane microneedles. *Proceedings of the ASME MEMS Device 2000 IMECE* 2, 355–359.
- Stupar, P.A., Pisano, A.P., 2001. Silicon, parylene, and silicon/parylene micro-needles for strength and toughness. In: *Proceedings of the 11th International Conference on Solid-State Sensors and Actuators*, Munich, Germany, pp. 1386–1389.
- Yamamoto, T., Yamamoto, Y., 1976. Electrical properties of the epidermal stratum corneum. *Medical Biology Engineering* 14, 151–158.
- Young, S.-T., Chan, K.H., Chen, C.F., 1987. An instrument using variation of resistance to aid in needle tip insertion in epidural block in monkeys. *Med. Instrum.* 21, 266–268.